

## Comparison of experimental and simulated extreme ultraviolet spectra of xenon and tin discharges

E. R. Kieft,<sup>\*</sup> K. Garloff, and J. J. A. M. van der Mullen<sup>†</sup>*Department of Applied Physics, Eindhoven University of Technology, P.O. Box 513, 5600 MB Eindhoven, The Netherlands*

V. Banine

*ASML Netherlands B.V., De Run 6501, 5504 DR Veldhoven, The Netherlands*

(Received 12 October 2004; published 11 March 2005)

Xenon and tin both are working elements applied in discharge plasmas that are being developed for application in extreme ultraviolet (EUV) lithography. Their spectra in the 10–21-nm-wavelength range have been analyzed. A fully analytical collisional-radiative model, including departure from equilibrium due to a net ionization rate, was used to simulate the EUV spectra. Detailed Hartree-Fock calculations, using the COWAN package, were applied for determination of the energy levels and optical transition probabilities of the 8+ to 12+ ions of both elements. For the calculation of the radiation, the opacity of the plasma was taken into account. Time-resolved measurements of the spectra from ionizing phases of two different discharge plasmas were corrected for the wavelength-dependent sensitivity of the spectrometer, and compared to the results of the simulations. Fairly good agreement between the experiments and the model calculations has been found.

DOI: 10.1103/PhysRevE.71.036402

PACS number(s): 52.65.-y, 32.30.Rj, 39.30.+w, 52.70.La

### I. INTRODUCTION

Discharge plasmas are currently regarded as the most promising concept for application as sources of high-power extreme ultraviolet (EUV) radiation in semiconductor lithography. Various types have been developed or are still under development by a number of groups in the world [1–8]. The working element in such a plasma has to be selected for its emission near 13.5 nm, since this is the wavelength for which the silicon/molybdenum (Si/Mo) multilayer mirrors in the optical system of the lithographic apparatus will be optimized. The two most popular elements are xenon and tin. Xenon has the advantage of being a noble gas, whereas tin is a solid at ambient conditions, and therefore might get deposited onto mirrors and other optical surfaces. However, tin is a much more efficient radiator at the desired wavelength. Other efficient radiators, such as oxygen and lithium, are less popular due to their chemical reactivity.

Since xenon and tin are both large, complex atoms, their spectra in the EUV range of roughly 10–21 nm do not consist of in sharp, well separated peaks, but rather form a quasicontinuum of a large number of peaks that cannot be resolved individually in a compact EUV spectrometer. The result of such a broad spectrum is that apart from the desired “in-band” radiation in a 2% wavelength band around 13.5 nm, also a large amount of out-of-band radiation is emitted. While this out-of-band radiation does not contribute to the illumination of the wafer in the lithography apparatus, it does contribute to the undesired heating of the discharge electrodes and the first optical elements in the system.

Therefore, from the application point of view, there is a desire to obtain detailed information on the shapes and in-

tensities of the EUV spectra of xenon and tin and insight into the mechanisms that determine the relative intensity of the in-band radiation.

EUV spectrometry can be applied to obtain information about the (time-resolved) spectra of xenon or tin in a discharge plasma. In our EUV laboratory at ASML, such experiments have been performed on two different types of discharge plasmas: a hollow cathode discharge in xenon [9] and a triggered vacuum arc in tin vapor [10]. Basic descriptions of the working principles of these two discharge plasmas are given in Refs. [7,9] and Ref. [10], respectively.

So far, the interpretation of the results has been performed without a detailed consideration of the wavelength dependency of the spectrometer sensitivity. Either the behavior of individual contributions to the spectrum was studied as a function of time during the pulse, or line intensities were compared among each other that were relatively close together in wavelength. In the latter case, a flat sensitivity curve for the spectrometer could be assumed without potentially making large errors. This assumption was supported by the fact that from theoretical considerations, no large deviations from a smooth curve (i.e., no sudden “jumps”) were to be expected. However, both for evaluating the effects of the spectrum emitted by the source on the mirror optics in a lithography tool, and for comparison with simulated EUV spectra, it was desirable that the theoretical considerations would be checked experimentally, and that the spectrometer sensitivity would be evaluated over the larger EUV wavelength range of (at least) 10–21 nm.

Studies of experimental EUV spectra and comparisons with simulations have been made in the past for various elements in different plasmas, including impurities in tokamaks. Examples are works on the spectra of tungsten [11,12], krypton and argon [13], and calcium [14], where the latter was aimed at benchmarking the analyses of solar spectra. The typical densities, temperatures, and lifetimes of to-

<sup>\*</sup>Electronic address: e.r.kieft@tue.nl

<sup>†</sup>Corresponding author. Electronic address: j.j.a.m.v.d.mullen@tue.nl

kamak plasmas are, however, quite strongly different from those of plasmas that are designed for application in EUV lithography.

Elaborate analyses of the latter have been presented previously by Gilleron *et al.* [15] for a laser-produced plasma (LPP) in a dense spray of droplets and Böwering *et al.* [16] for a dense plasma focus device. Both authors used xenon as the working element and have regarded only time-integrated EUV spectra, which complicates the interpretation of the results. Also, Gilleron uses a local thermal equilibrium (LTE) approach. Böwering claims to use a non-LTE approach, but still applies a simple Boltzmann factor for the emission from the excited states, which essentially results in the same shape of the spectrum. Although an LTE-like approach is appropriate for LPPs, it may give less accurate results for the less dense discharge plasmas. Both works take opacity effects into account to explain the high observed ratio of intensities between the features around 13.5 and 11 nm. However, for a correct evaluation of opacity effects it is essential to use a reasonably accurate description of line broadening, details of which can be found in neither of these works. Recently, Richardson *et al.* [17] have reported that they are working on a non-LTE radiation transport code for providing detailed spectra of laser-produced plasmas in xenon and tin.

The aim of this work is twofold. First, we present a theoretical and experimental investigation of our spectrometer sensitivity, so that we can obtain sensitivity-corrected spectra that are suitable for evaluation over larger wavelength ranges, and comparison with simulation results.

Second, we present a model which calculates the emitted EUV radiation from the ion density, electron temperature, size and geometry, and an effective net ionization rate of the plasma at a given time. The simulated spectra are matched, by variation of certain input parameters, to previously obtained experimental results which are now corrected for the spectrometer sensitivity. The aim is to obtain estimates for the main plasma parameters, and, more importantly, to gain insight in what mechanisms govern the population of excited states and the shapes and intensities of the radiated EUV spectra.

The spectral model was based on the radiation module of an existing model describing the evolution of laser-produced plasmas (LPPs) [18], but it was adjusted for the properties of discharge plasmas. The adjustments include the application of an analytical collisional-radiative model (CRM) for the calculation of excited state densities and more detailed calculations of line broadening and its influence on the opacity of the plasma. Also, an effective net ionization rate has been introduced to account for the fact that in an ionizing plasma, the ion stage distribution lags behind the instantaneous electron temperature. The plasma model, and the atomic data calculations which were used as input to the model, will be described in the following section.

In Sec. III, we will discuss the theoretical dependencies of the sensitivity of our EUV spectrometer on wavelength, and the sensitivity curve derived in this way will be compared to the results of an experimental calibration.

In Sec. IV, the results of the simulations for both the xenon and the tin source will be presented. Finally, in Sec. V, the simulated and experimental spectra will be compared, the

remaining differences will be discussed, and certain conclusions on the plasma properties will be drawn.

## II. SPECTRAL MODEL

### A. Radiation module

In Ref. [18], a computer model was described that simulates the evolution and radiation of a laser-produced plasma for generation of EUV radiation. Due to the modular design of the model, it was possible to separate the calculation of the radiation from the remaining parts of the model and to compile it into a separate executable file. The model requires as its input information on the geometry, chemical composition, total atom density, and electron temperature of the plasma. Also, atomic data for the elements present in the plasma are fed to the model in the form of input files.

From the total atom density and the temperature, first the electron density and the distribution of the species over the various ionization states is calculated self-consistently, based on an LTE assumption with Saha equilibrium for the population of the different ions. Second, the population densities for the excited states are calculated assuming Boltzmann distributions. As a next step, the model calculates the radiation emitted by the plasma. Finally, in the original model, the total radiation at each wavelength is cut off at the Planck level calculated over the total area of the plasma surface, at the given electron temperature. For this, the plasma is assumed to have a spherical shape. The output is written in the form of spectra over a certain wavelength range, giving the total radiation, the contributions from free-free (bremsstrahlung), free-bound (recombination), and bound-bound (line) radiation, and the radiation uncorrected for opacity effects.

For the work presented here, some changes have been made to the original radiation module to make it more appropriate for application to discharge plasmas, which typically have far lower electron densities than LPPs. In this section, these changes will be discussed in detail, first for the calculation of the distribution function of the ions over the ionization stages, then for the excited state densities, and next for the emitted radiation. Finally, a description will be given of the atomic data calculations leading to information about the energy levels and optical transition probabilities of the relevant ions.

### B. Ion densities

First of all, an analytical collisional radiative model (CRM) was introduced as an alternative to LTE for the calculation of the population densities of the various ions and excited states. The CRM is based for the largest part on the Corona model described in Refs. [19,20], which is valid for stationary and ionizing plasmas. In this model, the excited state density is given as a function of the effective principle quantum number (pqn)  $p$ , which is given by

$$p = Z \sqrt{\frac{Ry}{E_{\text{ion}} - E_{\text{exc}}(p)}}. \quad (1)$$

Here, the symbol  $p$  is used instead of the frequently used symbol  $n$  to avoid confusion with densities.  $Z$  represents the

charge number of the ion without the outermost electron, so that  $Z=z+1$ , with  $z$  being the charge number of the ion under consideration.  $Ry$ ,  $E_{\text{ion}}$  and  $E_{\text{exc}}(p)$  are the ionization energy of hydrogen, the ionization energy of the ion under consideration, and the energy of the excited state relative to the ground state, respectively. Some of the equations that are discussed below were originally derived for hydrogen atoms or hydrogenic ions in which the effective pqn and the actual pqn of an excited state are equal; however, with the appropriate adjustments they can also be applied as approximations for complex ions.

An important role is played in the CRM by the level  $p = p_{\text{cr}}$ , which is the boundary between radiative and collisional levels: for levels with  $p < p_{\text{cr}}$ , the decay is mainly radiative and we have a Corona-like balance, whereas for  $p > p_{\text{cr}}$ , it is mainly collisional, and we are in an *excitation saturation balance* (ESB). The position of this boundary level  $p_{\text{cr}}$  is determined by the criterion  $n_e K(p_{\text{cr}}) = A(p_{\text{cr}})$ , which means that for the critical level, the total collisional destruction equals the total radiative destruction. For the collisional destruction rate, Ref. [20] gives

$$K(p) = 6 \times 10^{-14} \text{ m}^3 \text{ s}^{-1} Z^{-2} p^4 \frac{\sqrt{T_e}}{T_e + 2Z^2} (1 + \varepsilon_p/4) \times \ln(2/\varepsilon_p + 1.3), \quad (2)$$

where  $T_e$  is the electron temperature in eV and  $\varepsilon_p = [E_{\text{ion}} - E_{\text{exc}}(p)]/kT_e$ . Note that by using a single electron temperature, we implicitly assume a Maxwellian electron energy distribution function (EEDF). In Sec. V, the validity of this approach for the plasmas under study will be verified.

In our calculations we use the above expression, but with two adjustments: first, we omit the  $Z^2$  scaling in the denominator, since distorted wave calculations [21] that we have performed for certain collisional excitation cross sections of  $\text{Xe}^{8+}$  ions do not seem to confirm the quasi-hard-sphere collision behavior for high values of  $\varepsilon_p$  in ions, as suggested in Ref. [20]. Also, we doubled the prefactor to account for the fact that in complex ions the typical energy distances between near-lying levels are smaller than in hydrogenic ions; this effect enhances the collisional destruction rate. The resulting expression is

$$K(p) = 1.2 \times 10^{-13} \text{ m}^3 \text{ s}^{-1} Z^{-2} p^4 \frac{\sqrt{T_e}}{T_e + 2} (1 + \varepsilon_p/4) \times \ln(2/\varepsilon_p + 1.3). \quad (3)$$

Further, for the radiative destruction rate we use

$$A(p) = \gamma Z^4 p^{-5} (3 \ln p - 2 \ln p_1 - \zeta) \quad (4)$$

in which  $\gamma = 7.87 \times 10^{-9} \text{ s}^{-1}$ ,  $p_1$  is the effective pqn of the ground state of the ion, and the opacity-dependent parameter  $\zeta$  equals 0.25 for the optically open case. Here, the expression from Ref. [20] was adjusted to account for the fact that  $p_1 > 1$  for ions that carry more than two electrons, and excited states cannot radiate to levels which have an effective pqn below that of the ground state of the ion.

The critical level is thus given by

$$p_{\text{cr}}^9 = 6.6 \times 10^{22} n_e^{-1} Z^6 \frac{T_e + 2}{\sqrt{T_e}} \left( \frac{3 \ln p_{\text{cr}} - 2 \ln p_1 - 0.25}{(1 + \varepsilon_p/4) \ln(2/\varepsilon_p + 1.3)} \right) \quad (5)$$

with the electron density  $n_e$  in units of  $\text{m}^{-3}$ . A further simplification is made by setting the value of the expression between brackets in Eq. (5) equal to 1.5, which turns out to be a reasonable value for the simulations in this study.

A further parameter used in this work is  $p_{\text{hc}}$ , which determines whether collisional excitation processes or deexcitation processes are dominant, and is given by

$$p_{\text{hc}} = Z \sqrt{Ry/(3kT_e)}. \quad (6)$$

For  $p > p_{\text{hc}}$ , the ESB is called *hot*, otherwise it is *cold*.

Now, the distribution over the subsequent ionization stages is derived from a balance between collisional ionization, radiative recombination, three-particle recombination, and an effective net ionization rate, in the following manner:

$$\frac{n_{z+1}}{n_z} = \frac{n_e S_z}{n_e \alpha_{r,z+1} + n_e^2 \alpha_{3p,z+1} + \nu_i}, \quad (7)$$

where  $S_z$  is the collisional ionization coefficient of the ion with charge number  $z$ ,  $\alpha_{r,z+1}$  is the radiative recombination coefficient of the next ion, and  $\alpha_{3p,z+1}$  is the three-particle recombination coefficient of that ion.  $\nu_i$  represents an effective net ionization rate, as explained below.  $n_z$  and  $n_{z+1}$  are the total densities of the ions with charge numbers  $z$  and  $z+1$ , respectively.

For the collisional ionization coefficient, we use a sum of the direct ionization coefficient of Vriens and Smeets [22]  $K(p_1, +)$  and the collisional excitation coefficients from the ground state to the different levels that are in hot ESB,

$$S_z = K_z(p_1, +) + \sum_{p=p_i, p_i+1, \dots, \leq 24} K_z(p_1, p) = K_z(p_1, +) + 1.6 \times 10^{-11} \text{ m}^3 \text{ s}^{-1} \sum_p \frac{f_{p_1 p} g(p_1, p)}{\Delta E \sqrt{T_e}} \exp(-\Delta E/kT_e), \quad (8)$$

in which  $p_i$  is the largest of  $p_{\text{cr}}$ ,  $p_{\text{hc}}$ , and  $p_1+1$ ;  $f_{p_1 p}$  is an analytical approximation for the optical oscillator strength of the transition, as given in Eq. (3.9) of Ref. [20],  $\Delta E$  is the excitation energy in eV of the level with pqn  $p$ . The gaunt factor  $g(p_1, p)$  is set equal to 0.16, where we use the fact that it approaches a constant value for near-threshold excitations in ions [23] and the numerical value was derived from the distorted wave calculations [21] as mentioned above.

By applying this ionization rate, we take into account that the stepwise excitation processes that finally lead to ionization are very fast compared to the first excitation to a level that is in hot ESB. Since both  $f_{p_1 p}$  and  $\exp(-\Delta E/kT_e)$  are rapidly decreasing functions of  $p$  for the relevant values of  $p$ , by far the largest contribution to  $S_z$  is formed by just the first term in the summation over  $p$ , and because typically  $p_i < 5$ , the cutoff for the sum,  $p \leq 24$ , does not have any appreciable effect on the result. Also, the calculations show that direct ionization contributes only a few percent to the total ioniza-

tion rates, so that the stepwise ionization process is dominant.

The three-particle recombination coefficient  $\alpha_{3p,z+1}$  is derived from the collisional excitation rate by imposing Saha equilibrium in the limit of high electron density; the radiative recombination coefficient  $\alpha_{r,z+1}$  was taken from Ref. [24] as cited in Ref. [25].

In discharge EUV plasmas, the time constants for reaching ionization equilibrium are typically not very small compared to the lifetime of the plasma, as discussed, e.g., in Ref. [26]. Therefore nonequilibrium effects during the ionization phase of the discharge will have a non-negligible effect on the distribution over the different ionization stages. The radiation module, being based on a quasi-steady-state assumption for the distribution of the ions, is not capable of taking these effects fully into account. However, to mimic the effect of an ionizing plasma, an optional additional parameter, the effective net ionization rate  $\nu_i$  was introduced, which can be interpreted as the time derivative of the average ion charge number  $z_{av}$ . The value of  $\nu_i$  compared to the recombination rates of the different ions is an indication of the relative importance of the ionization nonequilibrium.

### C. Excited state densities

After the densities of the different ions have been calculated, the population densities of the excited states are determined. These are expressed as an overpopulation compared to the Saha density, which is given by

$$\eta_z^S(p) = \eta_{z+1}(p_{1,z+1}) \frac{1}{2} n_e \frac{h^3}{(2\pi m_e k T_e)^{3/2}} \exp[(E_{ion} - E_{exc})/kT_e]. \quad (9)$$

Here,  $\eta_z(p)$  stands for the density per statistical weight of the levels with effective pqn  $p$ , and hence  $\eta_{z+1}(p_{1,z+1})$  represents the density per statistical weight of the ground state of the ion with charge number  $z+1$ . For  $p < p_{cr}$ , we are in the Corona domain. Here, the overpopulation of the excited level is expressed as a fraction of the overpopulation of the ground state [based on Eq. (9.6) in Ref. [20]]:

$$b(p) - 1 \equiv \frac{\eta(p) - \eta^S(p)}{\eta^S(p)} = (b_1 - 1) \max\left(\frac{n_e K(p, p_1)}{A(p)}, 1\right), \quad (10)$$

where  $b_1 - 1$  is the normalized overpopulation of the ground state, which is derived from the actual ratio of  $z$  to  $z+1$  ground state densities that follows from Eq. (7), compared to the Saha ratio (9). The expression contains both the collisional deexcitation to the ground state  $K_z(p, p_1)$  and the total radiative deexcitation  $A(p)$ . The collisional deexcitation rate is given by

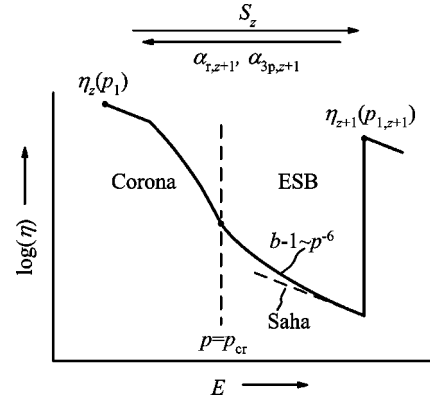


FIG. 1. A schematic plot of the densities per statistical weight as a function of the excitation energy. The positions of the Corona and ESB domains are indicated relative to  $p_{cr}$ . The arrows at the top indicate the directions of the ionization and recombination processes, as explained in Sec. II B.

$$K(p, p_1) = 1.6 \times 10^{-11} \text{ m}^3 \text{ s}^{-1} \frac{f_{pp_1} g(p_1, p)}{\Delta E \sqrt{T_e}} \\ \approx 3.0 \times 10^{-13} \text{ m}^3 \text{ s}^{-1} \frac{p_1^5}{Z^2 p^5 y^4 \sqrt{T_e}}. \quad (11)$$

Here,  $y = 1 - p_1^2/p^2$  is the ratio of the excitation energy to the ionization energy of the ion.

For the radiative decay, we use an approximation to Eq. (4):

$$A(p) = 1.3 \times 10^{10} \text{ s}^{-1} Z^4 p^{-4.5} \sqrt{1 - 2/p}, \quad (12)$$

valid for  $p > p_1 \approx 2.6$  for the relevant ions.

In the Corona domain, the relative overpopulation of an excited state compared to the Saha density (corresponding to Saha equilibrium with the ground state of the next ion) is now given by

$$b(p) - 1 = (b_1 - 1) \max\left(2.3 \times 10^{-23} n_e \frac{p_1^5}{Z^6 y^4 \sqrt{T_e} p (1 - 2/p)}, 1\right). \quad (13)$$

This expression is a strongly decreasing function of the excitation energy for the energy levels and plasma conditions of interest in this work, so that radiating levels with lower energies are favored over levels with higher energies, compared to a Boltzmann (or Saha) distribution.

In ESB ( $p > p_{cr}$ ), the relative overpopulation to the Saha density is set proportional to  $p^{-6}$  [27]. The prefactor is adjusted such that the ESB density matches the Corona density for  $p = p_{cr}$ . In Fig. 1, the positions of the Corona and ESB domains are indicated in a schematic plot of the densities per statistical weight as a function of the excitation energy.

### D. Radiation

The calculation of the broadening of each individual line was adjusted to include the effects of natural and Doppler broadening. The line profile is now calculated as a pseudo-

Voigt profile in which the Gaussian contribution corresponds to Doppler broadening and the Lorentzian part accounts for natural and Stark broadening. For the half width at half maximum of the Stark broadening contribution, the approximation of Eqs. (24) and (25) in Ref. [28] has been applied, which is given in frequency units by

$$w_{se} = 8 \left( \frac{\pi}{3} \right)^{3/2} \frac{\hbar}{m_e a_0} n_e \left( \frac{Ry}{kT_e} \right)^{1/2} \times \left[ \langle i|r^2|i \rangle \bar{g}_{se} \left( \frac{3kT_e}{2|\Delta E_i|} \right) + \langle f|r^2|f \rangle \bar{g}_{se} \left( \frac{3kT_e}{2|\Delta E_f|} \right) \right], \quad (14a)$$

with

$$\langle x|r^2|x \rangle = \frac{p_x^2}{2Z^2} [5p_x^2 + 1 - 3l_x(l_x + 1)] a_0^2. \quad (14b)$$

Here,  $x=i, f$  denotes either the initial or final state of the transition and  $\bar{g}_{se}(\xi)$  is an effective Gaunt factor, evaluated as

$$\bar{g}_{se}(\xi) = \max \left( 0.2, \frac{\sqrt{3}}{2\pi} \ln \xi \right). \quad (15)$$

As an order-of-magnitude approximation of the energy distance to the nearest perturbing level the expression  $|\Delta E| = \frac{1}{2} Z^2 Ry [1/p^2 - 1/(p+1)^2]$  is used, where the prefactor  $1/2$  is included to account for the fact that compared to a purely hydrogenic ion, the distance to the nearest perturbing level will be reduced due to the fine structure in combination with the  $l$ -dependent quantum defect. We believe that such an approximation is sufficiently accurate because  $\bar{g}_{se}(\xi)$  is only a very weak function of its argument.

To evaluate Eq. (14a) for every line, the  $l$  value of each relevant energy level has been included in the atomic data input files to the model.

The cutoff procedure for calculation of opacity effects was replaced by a somewhat more sophisticated method, in which the part of the radiation that escapes the plasma approaches the blackbody limit exponentially at each wavelength as the total emitted radiation increases. Again, the blackbody limit was evaluated over the entire surface area of the plasma, but the geometry of the plasma was changed from spherical to cylindrical, to better match the shape of a discharge plasma. Finally, the resulting emission can be convoluted with a Lorentzian-shaped spectrometer profile for easier comparison with experimental results.

### E. Atomic data

A faithful representation of the EUV spectra of both xenon and tin requires detailed information on the fine structure of energy levels of their ions, and transition probabilities for the main optical transitions between the excited and ground states. Such information was obtained from atomic data calculations using the COWAN package [29].

For both xenon and tin, the 8+ to 12+ ions are the main contributors to the EUV spectrum in the 10–21-nm-wavelength range. For these ions, apart from the  $4d^n$  ground

state configuration, also the  $4d^{n-1}5s, 6s, 5d, 5p, 6p, 4f$ , and  $5f$ , and  $4p^5 4d^{n+1}(pd)$  configurations were included in the calculations. Exceptions are  $Xe^{8+}$ , for which the  $pd$  configuration does not exist due to a full  $4d$  shell, and  $Xe^{12+}$ , for which the  $6s$  and  $6p$  configurations were omitted. On the other hand, the  $7p$  configuration was also included for  $Sn^{8+}$  and  $Xe^{8+}$ , the  $6f$  configuration was included for  $Xe^{8+,9+}$ . Similar calculations have also been performed for lower and higher stages of both elements. However, since the simulations show that these play minor roles in the plasmas, these are not discussed in detail here.

Relativistic terms were included in the calculations, and the Coulomb integrals were scaled down to 0.85 times their original values to account for weak interactions with other configurations.

To reduce file sizes and save calculation time, some of the weakest optical transitions were removed. All lines with an optical transition probability  $gA$  larger than  $10^8 \text{ s}^{-1}$  and  $3 \times 10^9 \text{ s}^{-1}$  for xenon and tin, respectively, were retained, and saved to input files for the radiation module described above. For all ions, the transition probability of the strongest line was at least about four orders of magnitude larger than the cutoff value.

## III. EUV SPECTROMETER SENSITIVITY

### A. Theoretical dependencies on wavelength

In the ASML EUV laboratory, a grazing incidence vacuum ultraviolet (vuv) spectrometer from ISAN, Troitsk (Russia), combined with a multichannel plate (MCP) detector and a digital camera, has been used in the experiments for recording of EUV spectra. In this section, first the theoretical considerations regarding the wavelength dependency of the sensitivity of this spectrometer will be briefly discussed, and a theoretical sensitivity curve will be constructed. After that, this curve will be compared to the results of an experimental wavelength-dependent sensitivity calibration.

The grating that was used for the recording of the EUV spectra has a ruling of 1200 l/mm and a blaze angle of  $1^\circ$ . It consists of a substrate covered with a 60-nm-thick gold coating and was used at a grazing angle of incidence of  $4^\circ$  and an angle of refraction of about  $10^\circ$  (depending on the wavelength). In the calculation of the theoretical efficiency of the spectrometer, four different factors should be taken into account:

(i) The geometrical efficiency of the spectrometer, given the groove density, the angle of incidence (and, connected to that, the angle of refraction) and the blaze angle,

(ii) the EUV reflectivity of gold at a grazing incidence angle of  $5^\circ$ ,

(iii) the inverse wavelength dispersion at the surface plane of the MCP detector (a larger spread of the signal will result in a lower signal per camera pixel), and

(iv) the wavelength-dependent sensitivity of the MCP.

The latter depends on the responsivity of the photocathode of the MCP, onto which a thin layer of gold has been deposited. From the literature on this subject [30] it is known that the gold photocathode efficiency strongly depends on

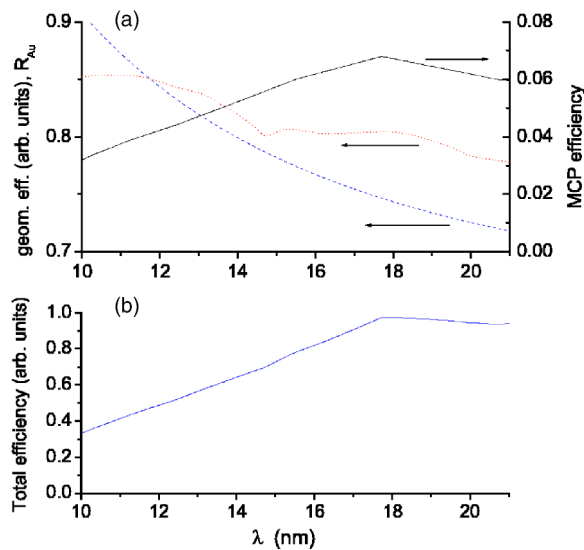


FIG. 2. (a) Geometrical spectrometer efficiency (dashed curve), 5° grazing-incidence gold reflectivity (dotted curve), and MCP efficiency (solid curve). (b) The total energy conversion efficiency of the spectrometer as a function of wavelength.

the degree of surface contamination. Since usually no special measures are taken in the handling of the MCP (for example, it is regularly exposed to air between experiments, and pumped down to a vacuum of only about  $1 \times 10^{-5}$  mbar, without any bake-out procedures), a contaminated surface was assumed. The quantum efficiency was copied from the data of Ref. [31] as quoted in Ref. [30].

The gold reflectivity was taken from the CXRO website on x-ray interactions with matter [32]. The geometrical efficiency combined with the inverse wavelength dispersion, the gold reflectivity, and the MCP efficiency for the EUV range are shown in Fig. 2(a). The combined effect of all three factors can be divided by the incident photon energy to get the total (relative) energy conversion efficiency as shown in Fig. 2(b).

### B. Experimental validation

The calibration of the wavelength dependency of the spectrometer for the EUV range was carried out by comparing pulse-integrated EUV spectra from the hollow cathode source with signals from a copy of the Flying Circus (FC) tool [33]. The original FC tool was designed in cooperation between the research organization FOM and the companies Philips and ASML, with the goal to set a standard for the measurement of in-band powers of EUV sources from different potential suppliers, so that a reliable comparison between those sources could be made. The name of the tool was derived from the fact that it was actually transported to various locations for measurements. In the FC tool, (EUV) radiation is wavelength filtered by reflection off a multilayer mirror and transmission through a thin foil filter, before it is collected on a photodiode. The FC has two channels. In our experiments, one of them was always equipped with a curved multilayer (ML) mirror designed for 13.5-nm wavelength. In the mirror holder for the second channel, for each

individual measurement a different flat ML mirror from PhysTex, that was optimized for a different wavelength, was placed. In total, measurements for eight different wavelengths have been done.

For each measurement, the pulse-integrated signals for both photodiodes were averaged over four discharge pulses of the source. Simultaneous to the measurement of the FC signal, a spectrum for the same pulses was recorded using the EUV spectrometer. The MCP was gated on a time scale long enough to record the total EUV emission for each pulse. The recorded spectrum was processed in the same way as in previous experiments.

Then, the spectrum was multiplied at each wavelength with the known photodiode sensitivities, filter transmission, mirror reflectivities, and aperture cross sections for both channels of the FC tool. Next, the results for both channels were integrated over wavelength. The resulting numbers are

$$I_{c1} = \pi r_1^2 \int_{10}^{21} J_\lambda(\lambda') R_1(\lambda') T(\lambda') \eta_{\text{diode},1}(\lambda') d\lambda', \quad (16a)$$

$$I_{c2,\lambda} = \pi r_2^2 \int_{10}^{21} J_\lambda(\lambda') R_2(\lambda') T(\lambda') \eta_{\text{diode},2}(\lambda') d\lambda'. \quad (16b)$$

Here,  $r_1$  is the radius of the curved mirror aperture,  $r_2$  is the filter radius of the second channel,  $T$  is the transmission of each filter, and  $R_i$  and  $\eta_{\text{diode},i}$  are the mirror reflectivity and the diode energy conversion efficiency of channel  $i$  ( $i=1,2$ ), respectively.  $J_\lambda(\lambda')$  are the raw spectrometer data, where  $\lambda'$  is given in nm.  $I_{c1}$  and  $I_{c2,\lambda}$  represent the calculated signals of the first and second channel, respectively. Now, if the spectrometer would have a flat sensitivity curve, the ratio of these two numbers would be equal to the ratio of measured FC signals. The difference between the two ratios therefore gives information about the relative sensitivity of the EUV spectrometer, in the following way:

$$\frac{I_{c2,\lambda}}{I_{c1}} = \frac{\eta_\lambda}{\eta_{13.5 \text{ nm}}} \frac{I_{m2,\lambda}}{I_{m1}}, \quad (17)$$

where  $I_{m1}$  and  $I_{m2,\lambda}$  represent the measured values from the first and second channel, respectively, and finally  $\eta_\lambda / \eta_{13.5 \text{ nm}}$  is the spectrometer efficiency at wavelength  $\lambda$ , relative to the sensitivity at 13.5 nm.

To partially eliminate some uncertainties in the filter transmissions and diode sensitivities, the end results were normalized using measurements in which both mirror holders of the FC held 13.5-nm mirrors. The results obtained in this way are summarized in Fig. 3. The square blocks represent the measured data; for the open squares, the two photodiodes were exchanged compared to the solid squares. The solid curve in the figure represents the theoretically constructed sensitivity curve as discussed above, normalized to unity at 13.5 nm. As the plot shows, there is a quite large spread between the sensitivity values of the individual data points. However, the experimental data do seem to confirm the general trend of the theoretical prediction; at least no large systematic deviation from the theoretical curve can be

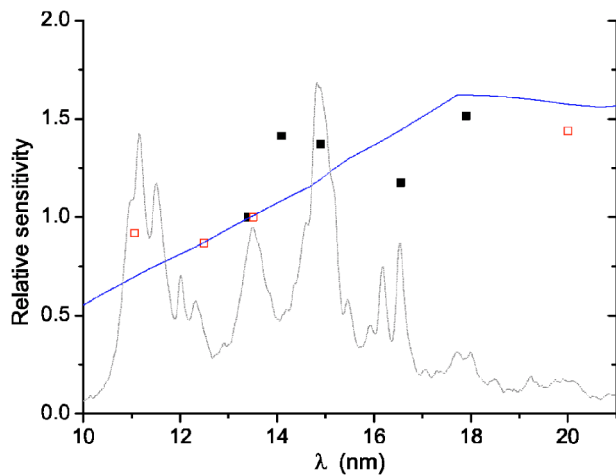


FIG. 3. Spectrometer sensitivity relative to 13.5 nm as derived using the Flying Circus method. The square blocks represent experimental results; for the open squares, the two photodiodes were exchanged compared to the solid squares. The solid curve represents the theoretical sensitivity (adjusted to match the scale). A representative time-integrated, measured xenon spectrum (dotted curve) is shown for reference.

detected. The relatively large differences between individual data points and the theoretical curve can probably be ascribed to the large uncertainties in filter transmission, diode sensitivity, and especially the mirror reflectivity. The experimental results in the remainder of this paper have been corrected using the theoretical curve as described above.

#### IV. SIMULATED EUV SPECTRA

For both the tin and xenon discharge plasmas, three different spectra have been selected from existing experimental results to be used as a basis for matching the model simulations. In the case of the xenon discharge, the same set of data as discussed in Ref. [9] has been applied. These are spatially integrated, but time-resolved, spectra recorded from the axial direction of the electrode geometry. The three spectra, to be referred to as (A), (B), and (C), correspond to timings roughly 20, 10, and 0 ns before the pinch. For the tin discharge, three spectra were selected from the data discussed in Ref. [10]. These are space- and time-resolved spectra, recorded from a direction perpendicular to the axis of symmetry of the discharge. The signals from an area between 0.1 and 0.45 mm from the cathode have been integrated. The spectra (D), (E), and (F) were recorded for timings of 40, 20, and 0 ns before the pinch. In both cases, signals from multiple pulses (30 and 10 for the xenon and tin discharges, respectively) were added to obtain more accurate results.

An automated fitting procedure of the model results to the experimental data would have become far too involved; also, the accuracy of the experimental results would not always have allowed for such a procedure. Therefore an alternative approach was followed. For the model calculations, we started with certain initial guesses for the ion density, electron temperature, plasma geometry, and the effective rate of ionization  $\nu_i$ , derived from pinhole images [9,10] and Thom-

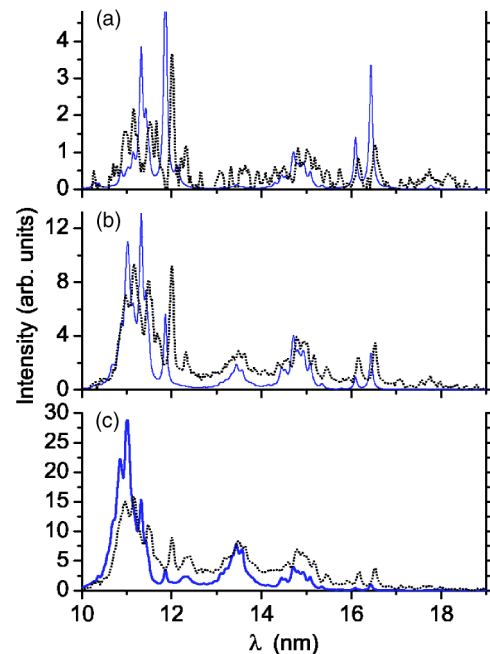


FIG. 4. Comparison of experimental xenon spectra (A), (B), and (C), as defined in the text (dotted curves) with simulation results (a), (b), and (c) (solid curves). The units for the scales of the three different plots are equivalent, and the ratios between the scales of the experimental and simulated results were kept fixed.

son scattering [34] results, where available. Next, these values were varied until a reasonable agreement, to the eye, between simulation and experiment was achieved. In doing so, however, the length of the plasma cylinder was not changed. Also, the values for the total ion density and the plasma radius were chosen such that the total number of ions in each plasma was roughly preserved for the different spectra of each type of discharge; the applied values were about  $1.3 \times 10^{14}$  and  $6 \times 10^{13}$  for the xenon and tin plasmas, respectively. In other words, the total number of ions in each type of plasma could only be changed for all three spectra simultaneously. This left just three parameters to be varied independently for each spectrum: the electron temperature  $T_e$ , the effective ionization rate  $\nu_i$ , and the plasma radius  $r$ .

The optimized simulated spectra will be referred to by the lower case equivalents (a)–(f) of the experimental spectra names (A)–(F). They are presented in Figs. 4 and 5, respectively. Even though the intensity units are in principle arbitrary, the same multiplication factors were used for different parts of each graph. Here, the simulated spectra were convoluted with a spectrometer profile with a full width at half maximum of 0.08 nm to make the model results better comparable to the experimental data. To demonstrate the effect of this convolution, the unconvoluted and convoluted versions of spectrum (f) are shown in Fig. 6 together with the blackbody radiation curve for the given plasma temperature and geometry. It can be seen that even though the convoluted spectrum stays well below the blackbody limit at all wavelengths, in the actual spectrum many lines do reach the blackbody limit.

For spectra (b) and (e), the contributions of the bound-bound radiation of the individual ions to the simulated spec-

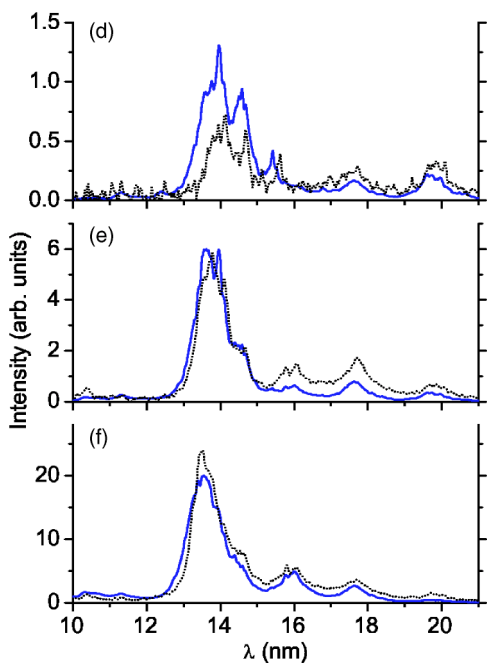


FIG. 5. Similar plots as in Fig. 4, but for the spectra of the tin discharge. Solid curves: simulated spectra (d), (e), and (f); dotted curves: experimental data (D), (E), and (F).

tra are plotted separately in Figs. 7 and 8, respectively. The individual contributions may not add up exactly to reproduce the spectra of Figs. 4 and 5, since in Figs. 7 and 8 first of all free-free and free-bound radiation are not included, and second, opacity effects were only considered for the individual contributions separately, so that overlaps of lines from different ions were not accounted for. As the figures show, for both xenon and tin the features corresponding to  $4d-4f$  and  $4p-4d$  transitions (around 11 and 14 nm, respectively) tend to overlap for different ionization stages, but on the other hand, the  $4d-5p$  arrays of the different ions are well separated, which makes identification of the different ions from an experimental spectrum possible. The contribution of  $\text{Sn}^{7+}$  is not shown in Fig. 8, but the COWAN calculations show that the

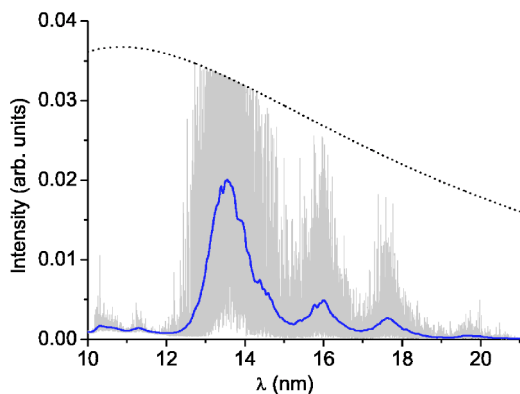


FIG. 6. Simulated spectrum (f) for the tin discharge, before (gray curve) and after (solid curve) convolution with a hypothetical spectrometer profile of 0.08 nm full width at half maximum. The dotted curve represents the blackbody limit under the applied input parameters of the model.

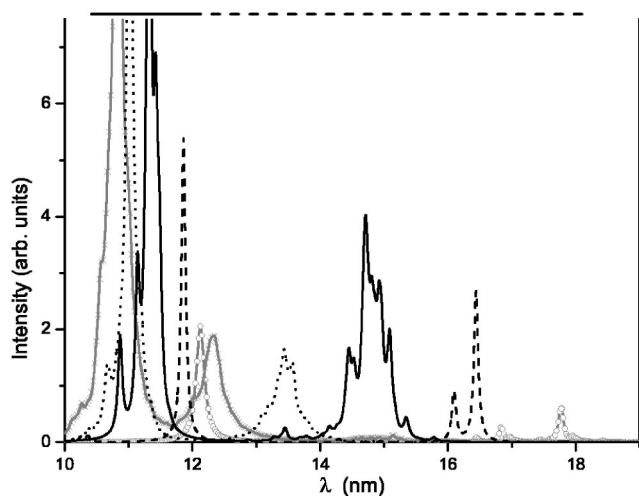


FIG. 7. The line radiation contributions of the individual ions  $\text{Xe}^{7+}$  (gray curve with open circles),  $\text{Xe}^{8+}$  (dashed),  $\text{Xe}^{9+}$  (solid),  $\text{Xe}^{10+}$  (dotted), and  $\text{Xe}^{11+}$  (gray curve with crosses) to the simulated xenon spectrum (b). The  $\text{Xe}^{7+}$  and  $\text{Xe}^{11+}$  curves have been magnified 15 times to make them visible on the same scale as the other ones. The solid horizontal line at the top of the graph shows the approximate position of the different  $4d-4f$  contributions, whereas the  $4d-5p$  contributions are indicated by the dashed line.

$4d-5p$  feature of this ion has its peak between 22 and 23 nm.

Details on the applied input parameters and the resulting electron densities and total radiation are given in Table I. These data suggest electron temperatures in the range of 23–27 eV for both plasmas, and electron densities up to about  $1 \times 10^{25}$  and  $3 \times 10^{25} \text{ m}^{-3}$  in the pinch phase for the xenon and tin plasmas, respectively.

An example of the effect of variation of parameters in general is given in Fig. 9. The parameters of the alternative

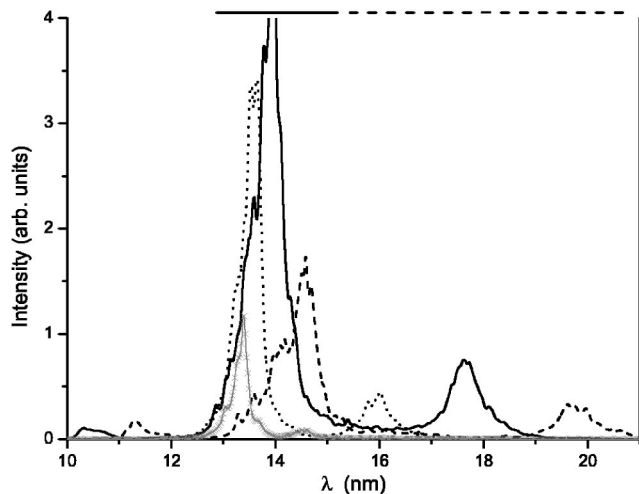


FIG. 8. The individual ion contributions of  $\text{Sn}^{8+}$  (dashed curve),  $\text{Sn}^{9+}$  (solid),  $\text{Sn}^{10+}$  (dotted), and  $\text{Sn}^{11+}$  (gray curve with crosses; magnified two times with respect to the other spectra) to the simulated tin spectrum (e). The solid horizontal line at the top of the graph shows the approximate position of the different  $4d-4f$  contributions, whereas the  $4d-5p$  contributions are indicated by the dashed line.

TABLE I. The input parameters and certain characteristics of the simulation results corresponding to the spectra shown in Figs. 4 and 5. Here  $n_i$  represents the total ion density,  $T_e$  is the electron temperature,  $\nu_i$  is the effective ionization rate, and  $r$  and  $l$  are the radius and length of the cylinder-shaped plasma, respectively. Further,  $z_{av}$  is the average ionization degree,  $n_e = n_i z_{av}$  is the electron density and  $I_{tot}$  represents the total energy emitted by the plasma in 5 ns time, in the wavelength range under consideration (10–21 nm for Sn, 10–19 nm for Xe).

Name	$n_i$ ( $10^{23} \text{ m}^{-3}$ )	$T_e$ (eV)	$\nu_i$ ( $10^7 \text{ s}^{-1}$ )	$r$ (mm)	$l$ (mm)	$z_{av}$	$n_e$ ( $10^{25} \text{ m}^{-3}$ )	$I_{tot}$ (mJ)
Xe (a)	1.35	24.5	4	0.55	1	8.32	0.112	3.0
Xe (b)	2.6	27	4.5	0.4	1	9.18	0.24	10.1
Xe (c)	10	25.5	1	0.2	1	9.86	0.99	24
Sn (d)	0.78	24	1.5	0.7	0.5	8.54	0.067	2.3
Sn (e)	3.1	23	3	0.35	0.5	9.21	0.29	9.1
Sn (f)	31.5	23	5	0.11	0.5	9.73	3.1	36
Sn (f1)	31.5	21	5	0.11	0.5	9.12	2.9	29
Sn (f2)	31.5	25	5	0.11	0.5	10.32	3.3	41

simulated spectra of Fig. 9 are included in Table I.

For the simulated spectra corresponding to the time of the pinch, the distributions over the ion stages are as follows: 2.6% of 8+, 28% of 9+, 51% of 10+, 16.9% of 11+, and 1.07% of 12+ for xenon; and for tin, 0.14% of 7+, 4.6% of 8+, 33% of 9+, 48% of 10+, 13.9% of 11+, and 0.80% of 12+. All the other ions give contributions of less than 0.1%. Since by far the most EUV radiation in each case is emitted by the plasma at the time of pinching, these simulations confirm that the ions mentioned above are the main contributors to the overall emission of both plasmas.

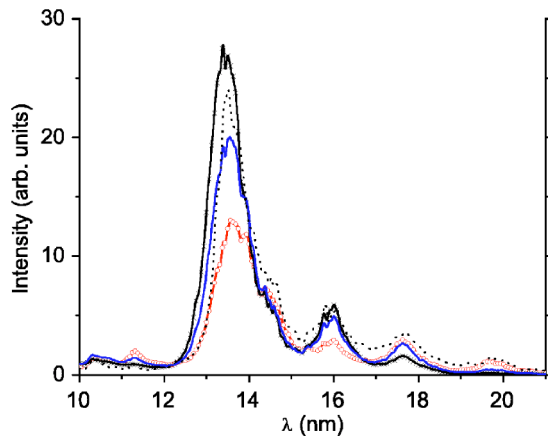


FIG. 9. Experimental tin spectrum (F) (dotted curve), and the corresponding simulation result (f) (solid curve) for  $T_e = 23$  eV. For comparison, alternative simulation results with  $T_e = 21$  eV (f1) (solid curve with open circles) and 25 eV (f2) (solid curve with crosses) have been included. Spectra (f1) and (f2) match the absolute intensity and the ratio of 13.5- and 17.5-nm peak intensities less well than the simulated spectrum (f), and they give incorrect ratios of intensities of the spectral features at 16 and 17.5 nm, indicating that the average ion charges for those simulations are wrong.

## V. DISCUSSION AND CONCLUSIONS

### A. Comparison of experimental and simulated spectra

Figures 4 and 5 show that there is quite good agreement between different aspects of the experimental results and the model calculations. This is especially true for the shapes and positions of the individual features of the spectra, which are basically a direct result of the atomic data calculations. In general, in these atomic data calculations the lines appear at slightly lower wavelengths than in the experiments. The effect seems to be the largest for the  $4d-4f$  transitions of different ions. This is not much different from what has been reported earlier [16,35–37].

Also, the absolute intensities of the simulated spectra compare well to experimental data. There is no direct absolute calibration available for the spectrometer, but the simulated in-band radiation (emitted in a 2% wavelength band around 13.5 nm) can be compared to power measurements that use a photodiode behind a Si/Nb filter and a multilayer mirror that also acts as a wavelength filter, such as in the Flying Circus in the case of the xenon source. Such measurements show that the total emitted in-band radiation per pulse is about 60 mJ for the tin source and 25 mJ for the xenon source, under the settings applied in this work. The simulated spectra for the pinch phase show in-band emission of 5.7 and 2.0 mJ, respectively, in 5 ns time. As experiments show that the typical effective durations for in-band emission are about 30 and 50 ns, respectively (taking experimental timing jitter into account), it can be concluded that the absolute in-band emission of both plasma EUV sources is reproduced rather well. The differences could be explained by the fact that the actual radiating volumes of plasma are somewhat larger than those assumed for the simulations.

Finally, the ratio of emission intensities of the  $4d-4f$  features compared to the  $4d-5p$  lines in the experiments is reproduced fairly well in the simulations. The COWAN code produces optical transition probabilities that are much larger for the  $4d-4f$  lines than for the  $4d-5p$  ones. Our calculations show that this difference is balanced for the largest part by

stronger opacity effects for the  $4d-4f$  lines, and the applied CRM, which relatively favors the population of the  $5p$  levels over the  $4f$  ones compared to a Boltzmann distribution. Still, the relative  $4d-4f$  intensities tend to be overestimated somewhat by the model; see the discussion below for possible explanations.

All this having been said, there are also some differences between the simulated spectra and the experimentally obtained ones. One notable effect that has been reported previously by other workers [16] is also seen here. This is the fact that, compared to the simulations, the experimental spectra seem to exhibit an additional broad, (quasi)continuum emission background that contributes strongly to the total emission in particular between the main emission features. Even though some of the weakest optical transitions were left out of our calculations, these are not strong enough to account for the difference. Another possible cause could be the underestimation of free-bound radiation in our work. However, our calculations show that the much (about 30–100 times) stronger free-bound contribution that would be needed to explain the observed difference, would also lead to a large emission feature at wavelengths below the main  $4d-4f$  emission peak for both elements. Such a feature has not been observed experimentally. A third explanation might be radiation emitted from doubly excited states. Such states have not been included in our calculations.

More generally, certain limitations in the model prohibit a better agreement between the simulations and the experiments. First of all, spatial variations in density, temperature, and optical density in the actual plasma can lead to observed spectra that cannot be simulated under the assumption of perfect homogeneity of the plasma. A zone of cooler plasma around the strongest EUV emitting region might, for example, absorb the  $4d-4f$  radiation relatively more than the  $4d-5p$  part. Also, a jitter in the timing of the experiments can lead to contributions of plasma with different properties to the same observed spectrum. Such an effect might, for example, have caused the apparently relatively strong  $4d-5p$  emission, which could be due to cooler, and hence more optically dense plasma, in spectrum (e) of the tin discharge. And finally, even though opacity of the plasma has been taken into account for the calculation of the radiation, its effect on the densities of excited states (a certain shift from Corona towards LTE balance, due to the decreased importance of radiative decay) has not been included. In view of the fact that both plasmas appear to be only partially optically dense, and the reasonably good results obtained with the current model, we believe that the error in the produced spectra made due to this omission is not very large.

A fundamentally different and far more elaborate approach would be required for a further improvement of the results. This approach would include a time- and ideally also space-dependent model of the evolution of the plasma, and a calculation of the population density of each excited state based on detailed information on optical transition probabilities, reabsorption of radiation and electronic (de-)excitation cross sections, rather than using analytical expressions that depend on the excited state energy only. However, such an approach was beyond the scope of this work.

## B. Validity of the single electron temperature approach

In Sec. II, we mentioned that we assume the electron energy distribution function (EEDF) to be Maxwellian. Here we will verify this assumption by discussing the influence of the main equilibrium disturbing processes for both extreme cases of lowest [spectra (A) and (D)] and highest [spectra (C) and (F)] electron densities. In discharge plasmas such as we are considering, the strongest processes to disturb a Maxwellian EEDF would be expected to be excitation of ions and acceleration due to the external electric field.

First we will evaluate the importance of ion excitation by comparing it to the equilibrium restoring process of energy redistribution due to electron-electron collisions. A good measure for the net effect of excitation of ions is the amount of emitted radiation, since the amount of energy “lost” to radiation is much larger than the amount of energy that is actually stored in the plasma in the form of excitation and/or ionization. From our experiments and simulations, it can be derived that the photon emission rates per free electron are roughly  $5 \times 10^7 \text{ s}^{-1}$  and  $5 \times 10^8 \text{ s}^{-1}$  for the lowest and highest density cases, respectively.

For the characteristic electron-electron collision rate for energy transfer, we use the equation for the case of a near-Maxwellian EEDF [38], given in numerical form by

$$\nu_e = 2.9 \times 10^{-12} \text{ m}^3 \text{ eV}^{3/2} \text{ s}^{-1} n_e \lambda T_e^{-3/2}, \quad (18)$$

where the value of the Coulomb logarithm  $\lambda$  is about 6 for the plasmas under consideration. Now,  $\nu_e$  is between  $1 \times 10^{11} \text{ s}^{-1}$  and  $2 \times 10^{11} \text{ s}^{-1}$  and between  $1 \times 10^{12} \text{ s}^{-1}$  and  $5 \times 10^{12} \text{ s}^{-1}$  for the low and high density cases, respectively. In both cases, the equilibrium restoring process is at least three orders of magnitude faster than the disturbing one, so that ion excitation is not capable of causing any significant deviation from a Maxwellian EEDF.

The importance of the external electric field can be derived from the magnitude of the electric current that is caused by it. From experiments as well as source design parameters, we know that the maximum current during the evolution of the discharge is about 20 kA. When we ignore the contribution of the ions, and divide this number by the elementary charge and the linear electron density in the direction of the current—which is about  $10^{18} \text{ m}^{-1}$  in all cases—we find an average directed electron velocity on the order of  $10^5 \text{ m s}^{-1}$ . The kinetic energy associated with this velocity, about 0.03 eV, is negligible in comparison with the electron temperatures that we have found. Therefore also the external electric field in the plasma does not lead to a significant deviation from a Maxwellian EEDF, and it can be concluded that, at least for the spectra that are the subject of this work, a description of the EEDF by a single electron temperature  $T_e$  is justified.

## C. Plasma properties

Considering the uncertainties in the spectrometer calibration, the aforementioned inherent limitations in the model, and the limited accuracy with which the simulated spectra could be matched to the experimental ones, the comparison of experimental and simulated spectra should not be viewed

as a way to obtain high accuracy data on plasma parameters such as electron densities and temperatures. However, it is a useful method to derive certain estimates for those parameters. More importantly, it is a way to evaluate which phenomena play an important role in determining the shapes and intensities of the EUV spectra.

It should be noted that it has proven possible to obtain reasonable agreement between experimental and simulated spectra using realistic values for all plasma parameters. The plasma dimensions match the results from pinhole imaging experiments fairly well, and the densities were chosen such that the total number of ions in the plasma remains roughly constant during the pinch evolution. For the xenon discharge, the initial ion density before pinching roughly corresponds to the background gas density if the initial radius of the plasma is taken to be about 4.5 mm, which is a realistic value given the geometry of the electrodes.

For spectra (d) and (e) of the tin discharge, the electron temperatures and densities can be compared to the results of Thomson scattering (TS) experiments [34]. The densities given there, about  $4 \times 10^{23}$  and  $1 \times 10^{24} \text{ m}^{-3}$ , respectively, are somewhat lower than the results presented here for the same time in the discharge evolution. However, the experimental jitter and the fact that the EUV emission increases strongly with time in this phase of the discharge may be responsible for this. Effectively, the EUV spectra will be more representative of the emission somewhat later in the discharge evolution, when the electron density is higher.

The electron temperatures derived from TS increase from about 17 to over 30 eV in the relevant time interval. The temperatures in Table I are in the same range, although they are much more constant as a function of time. It is worth mentioning that the TS measurements give three-dimensional spatially resolved data, whereas the spectrum simulations are based on measurements in which radiation from a certain cross section of the plasma is integrated, which might affect the effective temperatures. For the actual pinch phase of the tin discharge, no experimental data are available.

The values of the input parameter  $\nu_i$  are in agreement with the rate of increase of the average ion charge  $z_{av}$  to within roughly a factor 2. The difference for xenon is an indication that perhaps the ionization coefficient used in this model is still somewhat too low, in spite of the adjustments that have been introduced in Eq. (3).

The electron temperatures that were needed to get good agreement between the simulations and the experiments, are not extremely high:  $T_e$  was lower than 30 eV in all cases. Leaving out the ionization effect (i.e., setting  $\nu_i$  equal to zero), the electron temperatures required to obtain the same average ion charges, keeping all other input parameters the same, vary from 18 to 25 eV. The difference to the actual electron temperature decreases from about 6 to less than 1 eV, when going from the first to the last spectrum of each plasma. In other words, ionization effects should be taken into account; however, our results seem to indicate that they are not very strong, and the electron temperature is never more than a few eV higher than in the equilibrium case for the same average ion charge.

The importance of opacity to practical applications seems to depend on the type of plasma. As was mentioned above, the  $4d-4f$  lines were affected the most by reabsorption in the plasma in our model. For the xenon pinch plasma, also the intensity of the  $\text{Xe}^{9+}$   $4d-5p$  feature around 15 nm was strongly reduced by opacity. On the other hand, the  $4d-5p$  emission of  $\text{Xe}^{10+}$  around 13.5 nm was relatively unaffected. This is an indication that dilution of the plasma might perhaps be helpful to increase the energy conversion efficiency for the tin discharge, but not so much for the xenon discharge. Such a dilution would reduce the amount of energy needed to run the plasma, while keeping the level of emitted in-band radiation actually escaping from the plasma at a (nearly) constant level. It is only useful when the plasma is optically dense for at least a part of the wavelength range of interest.

Summarizing, we have shown that atomic and plasma physics calculations can result in fairly good reproduction of experimentally observed EUV spectra of discharge plasmas. To obtain a reasonable agreement, however, several factors have proven to be essential. These include first of all a correction for the wavelength dependency of the spectrometer sensitivity; and further an (albeit rough) treatment of ionization effects; a non-LTE approach to the population of the excited states of the ions; and a good description of the broadening mechanisms for the spectral lines, to account for opacity effects (especially during the pinch phase) in a correct manner.

- 
- [1] M. A. Klosner and W. T. Silfvast, *Opt. Lett.* **23**, 1609 (1998).  
 [2] S. R. Mohanty, C. Cachoncinlle, C. Fleurier, E. Robert, J.-M. Povesle, R. Viladrosa, and R. Dussart, *Microelectron. Eng.* **61-62**, 179 (2002).  
 [3] M. McGeoch, *Appl. Opt.* **37**, 1651 (1998).  
 [4] V. M. Borisov, I. Ahmad, S. Goetze, A. S. Ivanov, O. B. Khristoforov, J. Kleinschmidt, V. Korobotchko, J. Ringling, G. Schriever, U. Stamm, and A. Y. Vinokhodov, *Proc. SPIE* **4688**, 626 (2002).  
 [5] W. N. Partlo, I. V. Fomenkov, R. M. Ness, R. I. Oliver, S. T. Melnychuk, and J. E. Rauch, *Proc. SPIE* **4343**, 232 (2001).  
 [6] M. W. McGeoch and C. T. Pike, *Proc. SPIE* **5037**, 141 (2003).  
 [7] K. Bergmann, G. Schriever, O. Rosier, M. Müller, W. Neff, and R. Lebert, *Appl. Opt.* **38**, 5413 (1999).  
 [8] Proceedings of the EUV Source Workshop, International SEMATECH, Antwerp, Belgium, edited by V. Bakshi, 2003.  
 [9] E. R. Kieft, J. J. A. M. van der Mullen, G. M. W. Kroesen, and V. Banine, *Phys. Rev. E* **68**, 056403 (2003).  
 [10] E. R. Kieft, J. J. A. M. van der Mullen, G. M. W. Kroesen, V. Banine, and K. N. Koshelev, *Phys. Rev. E* **71**, 026409 (2005).  
 [11] R. Radtke, C. Biedermann, J. L. Schwob, P. Mandelbaum, and R. Doron, *Phys. Rev. A* **64**, 012720 (2001).  
 [12] K. Asmussen, K. B. Fournier, J. M. Laming, R. Neu, J. F. Seely, R. Dux, W. Engelhardt, J. C. Fuchs, and ASDEX Up-

- grade Team, Nucl. Fusion **38**, 967 (1998).
- [13] M. J. May, K. B. Fournier, D. Pacella, H. Kroegler, J. E. Rice, B. Gregory, M. Finkenthal, H. W. Moos, G. Mazzitelli, and W. H. Goldstein, Phys. Rev. E **61**, 3042 (2000).
- [14] V. A. Soukhanovskii, S. Lippmann, M. J. May, M. Finkenthal, H. W. Moos, K. B. Fournier, W. Goldstein, D. Pacella, and G. Mazzitelli, Astron. Astrophys., Suppl. Ser. **142**, 95 (2000).
- [15] F. Gilleron, M. Poirier, T. Blenski, M. Schmidt, and T. Cecotti, J. Appl. Phys. **94**, 2086 (2003).
- [16] N. Böwering, M. Martins, W. N. Partlo, and I. V. Fomenkov, J. Appl. Phys. **95**, 16 (2004).
- [17] M. C. Richardson, C.-S. Koay, K. Takenoshita, C. Keyser, S. George, S. Teerawattanasook, M. Al-Rabban, and H. Scott, Proc. SPIE **5374**, 447 (2004).
- [18] K. Garloff, M. van den Donker, J. J. A. M. van der Mullen, F. van Goor, R. Brummans, and J. Jonkers, Phys. Rev. E **66**, 036403 (2002).
- [19] J. J. A. M. van der Mullen, Ph.D. thesis, Eindhoven University of Technology, Eindhoven, 1986, <http://alexandria.tue.nl/extra3/proefschrift/PRF5A/8601253.pdf>
- [20] J. A. M. van der Mullen, Phys. Rep. **191**, 109 (1990).
- [21] Y.-K. Kim, MCDF on-line execution, <http://amods.kaeri.re.kr/mcdf/MCDF.html>
- [22] L. Vriens and A. H. M. Smeets, Phys. Rev. A **22**, 940 (1980).
- [23] H. van Regemorter, Astrophys. J. **136**, 906 (1962).
- [24] M. J. Seaton, Mon. Not. R. Astron. Soc. **119**, 81 (1959).
- [25] A. C. Kolb and R. W. P. McWhirter, Phys. Fluids **7**, 519 (1964).
- [26] M. Masnavi, M. Nakajima, and K. Horioka, J. Plasma Fusion Res. **79**, 1188 (2003).
- [27] T. Fujimoto, J. Phys. Soc. Jpn. **47**, 273 (1979).
- [28] H. R. Griem, Phys. Rev. **165**, 258 (1968).
- [29] R. D. Cowan, *The Theory of Atomic Structure and Spectra* (University of California Press, Berkeley, 1981) (code in a version for personal computers, edited by A. Kramida, at <http://das101.isan.troitsk.ru/cowan.htm>).
- [30] H. Henneken, F. Scholze, M. Krumrey, and G. Ulm, Metrologia **37**, 485 (2000).
- [31] R. H. Day, P. Lee, E. B. Saloman, and D. J. Nagel, J. Appl. Phys. **52**, 6965 (1981).
- [32] [http://www-cxro.lbl.gov/optical\\_constants/](http://www-cxro.lbl.gov/optical_constants/)
- [33] R. Stuik, H. Fledderus, P. Hegeman, J. Jonkers, M. Visser, V. Banine, and F. Bijkerk, in Proceedings of the Second SEMATECH Workshop on Extreme UV Lithography, San Francisco, 2002 (unpublished).
- [34] E. R. Kieft, J. J. A. M. van der Mullen, G. M. W. Kroesen, V. Banine, and K. N. Koshelev, Phys. Rev. E **70**, 056413 (2004).
- [35] S. S. Churilov and Y. N. Joshi, Phys. Scr. **65**, 40 (2002).
- [36] J. Blackburn, P. Carroll, J. Costello, and G. O'Sullivan, J. Opt. Soc. Am. **73**, 1325 (1983).
- [37] G. O'Sullivan, J. Phys. B **15**, L765 (1982).
- [38] B. A. Trubnikov, Rev. Plasma Phys. **1**, 105 (1965).